

Data-assisted CFD modeling of transient blast furnace tapping with a dynamic deadman

M. Vångö^a, C. Feilmayr^b, S. Pirker^{a,c}, T. Lichtenegger^{a,c,*}

^a Department of Particulate Flow Modelling, Johannes Kepler University, Linz, Austria

^b Ironmaking R&D, voestalpine Stahl GmbH, Linz, Austria

^c Linz Institute of Technology (LIT), Johannes Kepler University, Linz, Austria

ARTICLE INFO

Article history:

Received 19 December 2018

Revised 30 March 2019

Accepted 4 April 2019

Available online 15 April 2019

Keywords:

Computational fluid dynamics

Discrete element method

Volume of fluid

Decoupling of time scales

Blast furnace tapping

Transient deadman

ABSTRACT

The blast furnace (BF) hearth's condition is crucial for a long and healthy campaign life. Previous numerical investigations on BF drainage commonly treated the deadman as a static, porous medium. In this work, we employ a coupled computational fluid dynamics (CFD) – discrete element method (DEM) to account for its dynamic behavior. The model is utilized in several short-term simulations to generate a database of deadman states based on iron and slag levels, coke properties and the burden weight distribution. In contrast to the previous Eulerian deadman descriptions, we directly obtain an inhomogeneous description of the porosity from a particle size distribution. The database is utilized in the *dynamic void fraction model*, to describe the transient deadman in a fully Eulerian framework for long-term simulations. In essence, we present a strategy to mitigate the coupling between the dynamics of a packed bed and the fluid flow through it by connecting the bed's evolution to global state parameters such as the levels of liquids in which the particles float. This methodology is not restricted to blast furnaces, but can also be applied to other problems involving slow granular motion with dynamic interstitial fluids.

The model is first validated with experiments of water drainage through a lab-scale, particle-filled tank, and is shown to give similar results as CFD–DEM for both sitting and floating particle beds. We then demonstrate our model's advantages and necessity on isothermal simulations of a full-scale BF hearth for various deadman setups. We further highlight the effects of a coke free region due to a floating deadman as well as an almost impermeable dense center on the flow. Finally, by comparing simulations of a dynamic and a fixed floating deadman, we show that the dynamic behavior significantly affects the iron and slag drainage rate, which results in a 20 min extended duration after 120 min tapping.

To conclude, we present a highly performing approach to study the behavior of fluid flow through moving granular beds without costly contact detection but with information obtained from previous DEM simulations.

© 2019 Elsevier Inc. All rights reserved.

* Corresponding author at: Department of Particulate Flow Modelling, Johannes Kepler University, Linz, Austria.

E-mail addresses: mathias.vangoe@jku.at (M. Vångö), christoph.feilmayr@voestalpine.com (C. Feilmayr), stefan.pirker@jku.at (S. Pirker), thomas.lichtenegger@jku.at (T. Lichtenegger).

1. Introduction

A BF is in essence a giant cylindrical reactor used to reduce and smelt iron ore into liquid iron (hot metal) as part of the popular *blast furnace–oxygen steelmaking* process [1]. Iron ore and the reducing agent (coke) are charged in alternating layers from the top of the furnace, while oxygen enriched air (hot blast) is blown in from tuyeres located above the hearth at the lower part of the BF. The hot blast is transformed to reducing gas and forced upwards in the furnace, which removes oxygen from the iron ore before smelting it [1]. Molten iron (hot metal) and slag (a by-product of the production) drip downwards through the voids of the dense, porous structure of remaining coke particles (deadman) and settle in immiscible layers in the hearth. The rate of the hot metal melting is referred to as production rate throughout this work, with the amount of produced slag quantified as the specific slag ratio given in kilogram slag per ton hot metal (kg/thm). Finally, the liquids are retrieved through a taphole in a process often called BF tapping or casting, wherein a hole is drilled through the refractory. A BF with common terminology is schematically illustrated in Fig. 1 to aid the reader with the specific nomenclature.

The condition of the BF hearth has been proven to be critical to ensuring a stable operation and consequently, a long and healthy campaign [2,3]. Although the hot metal flow has a major influence on the hearth wear, direct measurements are difficult due to the harsh conditions. Hence, numerical methods are essential tools to provide knowledge of the hearth's state [4,5]. For an overview over modeling and simulation activities on the full blast furnace, we refer the interested reader to the review by Kuang et al. [6] and references therein.

Extensive research on BF hearth drainage was carried out in the past, but due to the complex flow situation, often very simple models were applied depending on the phenomena of interest. For example, steady-state simulations of the hot metal flow coupled with heat transfer models for the refractory were performed in Refs. [3,4,7–9]. Huang et al. [5] took the unsteady nature into account and simulated the transient behavior of the hot metal flow, which was also extended to take the slag layer into account [10–13]. Furthermore, the work done in Refs. [4,14] showed that temperature variations in the iron have significant influence on the flow due to natural convection.

Previous research commonly treated the deadman as a static porous medium, either uniform or with partly- or even fully impermeable areas. Alternatively, the deadman could be described with DEM, where the coke particles are modeled as discrete entities. DEM was widely used in studies of the solids flow in the BF with various foci of interest and complexity [15–23]. However, to the best of our knowledge, it had not found its way to detailed hearth tapping simulations until recently, even though we believe it provides a more accurate description of the deadman. Firstly, it gives rise to an inhomogeneous porosity description based on a given particle size distribution, and secondly in the case of an active deadman, it captures the effects of its dynamics. In our previous work [24], we employed a multiphase CFD–DEM model on a small-scale BF hearth, and highlighted the necessity to do so in the case of an active deadman. Despite the advantages of the model's level of detail, we pointed out challenges and limitations regarding simulations of an industrial-scale BF. Most importantly, DEM becomes computationally extremely expensive for large amounts of particles. Since the employed volume of fluid (VOF) method sets an upper limit on the choice of cell size in order to have a meaningful interface representation, common scale-up procedures in DEM, e.g. coarse graining [25,26], are not directly applicable to reduce the number of grains. While this problem might be tackled with the recent technique of locally confined coarse graining [27,28], small time steps inherent to DEM severely restrict the possible time range to be simulated. Thus, straight-forward usage of CFD– or VOF–DEM is not suitable for full-scale BF simulations to achieve results on realistic time scales.

In this work, we present a model intended to bridge the gap between the fast, Eulerian, static deadman simulations and the computationally expensive, accurate CFD–DEM ones. The CFD–DEM model provides us with detailed descriptions of the spatial porosity distribution based on actual, local particle sizes. Connecting each of the generated porosity fields with specific liquid levels, we subsequently obtain a simplified model for the deadman movement depending on the amounts of iron and slag currently present. Intrinsicly, the model aims to diminish the coupling between packed bed dynamics and fluid flow in the presence of strongly separated time scales. Some of us have suggested a similar approach in Ref. [29],

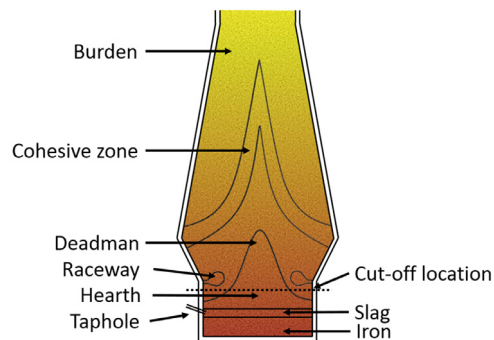


Fig. 1. Illustration of a blast furnace highlighting the conventional terminology. The present work focuses on the hearth, the region below the dotted line, while other parts like the raceways, the cohesive zone or the burden are not treated explicitly.

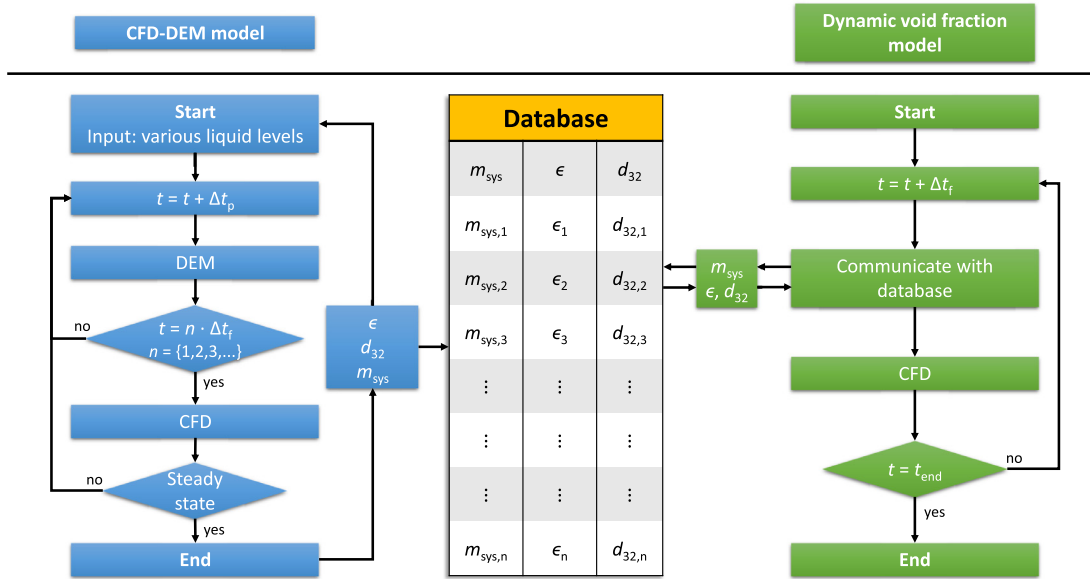


Fig. 2. Visualization of the interaction between the CFD–DEM model and the dynamic void fraction model. The CFD–DEM model is used to generate different deadman states $\{\epsilon_i(\mathbf{r}); d_{32,i}(\mathbf{r})\}$ related to the liquid levels by m_{sys} , which are utilized by the dynamic void fraction model in a fast long-term simulation.

where we time-extrapolated the evolution of a highly dynamic system based on an iterated method of analogues [30]. While in that work, recurrences of states were available from a recurrence statistics [31] prior to the simulation, in the present manuscript, they are determined from calculation results at runtime. We stress that the model is not restricted to blast furnaces, but is applicable to general systems of fluids in slowly moving granular media where the latter’s motion can be related to global state parameters. Ultimately, this enables us to go far beyond the limitations of the underlying CFD–DEM model. Throughout this work, we utilize the open-source software *OpenFOAM*, *LIGGGHTS* [32] for the CFD and DEM calculations respectively, together with the CFD–DEM coupling framework *CFDEMcoupling* [33].

With a much faster simulation tool and consequently longer investigated process times available, we also need to address the issue of slowly changing properties and parameters. In particular, we describe the gradual variation of the taphole as found in a real BF by accounting for its time-dependent length and diameter in terms of a simple boundary condition.

The paper is organized as follows. Firstly, we present the computational models used as well as our proposed boundary conditions (Section 2), followed by a model validation (Section 3). Lastly, we demonstrate the usage and advantages of the proposed dynamic void fraction model on a full-scale isothermal example BF for various deadman conditions (Section 4).

2. Computational model

In this work, two computational approaches, a CFD–DEM and a *dynamic void fraction model* are used. Due to its computational effort, the former is limited to short-term investigations to generate inhomogeneous representations of the deadman. Its position, shape and porosity distribution are obtained for a given burden load and particle size distribution. By performing several short-term simulations of various hot metal and slag levels without drainage, a database (“deadman database”) is assembled wherein the steady state spatial distribution of porosity and the Sauter-mean-diameter are stored as cell values, along with the corresponding global fluid mass in the system. With this approach, we neglect the influence of the drag force on the particle phase and retain only buoyancy.

Instead of solving each grain’s equation of motion including expensive particle contacts and collisions, the dynamic void fraction model retrieves global, solid phase configurations from the database of the pre-generated deadman states. This enables us to simulate several hours real-time of an industrial scale BF hearth, while accounting for the moving deadman in a simplified manner by sacrificing information about the individual particle movements. The interaction between the models is shown schematically in Fig. 2.

2.1. CFD–DEM governing equations

The discrete particles in the CFD–DEM model are governed by Newton’s laws of motion

$$m_i \frac{d\mathbf{u}_{p,i}}{dt} = \mathbf{F}_i^{pp} + \mathbf{F}_i^{pf} + m_i \mathbf{g} \quad (1)$$

$$I_i \frac{d\omega_{p,i}}{dt} = \mathbf{M}_i^{pp} \tag{2}$$

based on the theory of Cundall and Strack [34], where $\mathbf{u}_{p,i}$ is the particle translational and $\omega_{p,i}$ the angular velocity [35]. \mathbf{F}_i^{pp} denotes the inter-particle forces [36] which are approximated with a spring-dashpot method [37], in which the elastic spring and viscous damping coefficients are related to the physical material properties as given in Refs. [38,39]. Furthermore, the walls are treated as particles with infinite radius and assumed to have similar material properties for determining the particle-wall contact behavior. \mathbf{F}_i^{pf} describes the particle–fluid interaction force which we estimate with the presumably dominant drag, pressure gradient and viscous forces [40].

The continuous fluid phases are modeled with the VOF method [41]

$$\frac{\partial \epsilon \alpha_i}{\partial t} + \nabla \cdot (\epsilon \alpha_i \mathbf{u}_f) - \nabla \cdot (\mathbf{u}_c \alpha_i (1 - \alpha_i)) = 0 \tag{3}$$

$$\frac{\partial \epsilon}{\partial t} + \nabla \cdot (\epsilon \mathbf{u}_f) = 0 \tag{4}$$

$$\frac{\partial \epsilon \rho_f \mathbf{u}_f}{\partial t} + \nabla \cdot (\epsilon \rho_f \mathbf{u}_f \mathbf{u}_f) = -\epsilon \nabla p^* + \epsilon \nabla \cdot \boldsymbol{\tau} - \epsilon \mathbf{g} \cdot \mathbf{x} \nabla \rho_f + \epsilon \mathbf{F}^\sigma + \mathbf{F}^{pf}, \tag{5}$$

where Eq. (3) is the volume fraction advection equation for fluid phase i and Eqs. (4) and (5) the Navier-Stokes equations with incorporated void fraction ϵ due to the solids phase [42]. Here, α_i denotes the volume fraction of fluid phase i , \mathbf{u}_f the fluid velocity, ρ_f the fluid mixture density, \mathbf{g} gravity and \mathbf{x} the coordinate vector. Eq. (5) is solved using the non-hydrostatic pressure p^* defined as $p^* \equiv p - \rho_f \mathbf{g} \cdot \mathbf{x}$, in which the third term on the right hand side arise from the hydrostatic part (for a detailed description cf. Ref. [43]). Furthermore, the third term on the left hand side of Eq. (3) represents the interface compression in which \mathbf{u}_c denotes the compression velocity. This term acts to sharpen the fluid interfaces by counteracting the excessive numerical diffusion occurring in its vicinity [43]. Moreover, $\boldsymbol{\tau}$ is the stress tensor which reads

$$\boldsymbol{\tau} = \mu_f (\nabla \mathbf{u}_f + \nabla \mathbf{u}_f^T) - \frac{2}{3} \mu_f \mathbf{I} \nabla \cdot \mathbf{u}_f \tag{6}$$

for a Newtonian fluid, where μ_f is the fluid mixture dynamic viscosity. Fully laminar flow was assumed throughout this work. Additionally, \mathbf{F}^σ represents the surface tension force which is modeled with the well-known CSF (continuum surface force) model by Brackbill et al. [44]. For a complete description of the CFD–DEM model cf. Ref. [24].

2.2. Dynamic void fraction model

Similarly to the CFD–DEM model, the fluid flow in the dynamic void fraction model is described by Eqs. (3)–(5). However, Eqs. (3) and (4) are extended with the source term S_p as

$$\frac{\partial \epsilon \alpha_i}{\partial t} + \nabla \cdot (\epsilon \alpha_i \mathbf{u}_f) - \nabla \cdot (\mathbf{u}_c \alpha_i (1 - \alpha_i)) = S_{p,i} \tag{7}$$

$$\frac{\partial \epsilon}{\partial t} + \nabla \cdot (\epsilon \mathbf{u}_f) = S_p, \tag{8}$$

to account for the production rate of iron and slag, in which $S_p = \sum S_{p,i}$. It is represented by a constant iron production rate \dot{m}_{iron} and slag ratio γ , evenly distributed among the cells containing the respective phase as

$$S_{p,i} = \begin{cases} S_{p,\text{iron}} = \Theta(\alpha_{\text{iron}} - 1) \dot{m}_{\text{iron}} / (\rho_{\text{iron}} V_{\text{iron}}) \\ S_{p,\text{slag}} = \Theta(\alpha_{\text{slag}} - 1) \gamma \dot{m}_{\text{iron}} / (\rho_{\text{slag}} V_{\text{slag}}), \end{cases} \tag{9}$$

where the Heaviside function Θ restricts the term to regions with $\alpha_i = 1$ and $V_{\text{iron}; \text{slag}}$ representing their total volumes. This is done in order to preserve separation of the phases and thus retain sharp interfaces. The source term in Eq. (7) is required to account for the displacement caused by the general mass source S_p in Eq. (8) and the accompanying local pressure increase.

As the DEM part is not included in this model, special treatment is required for ϵ and \mathbf{F}^{pf} . The void fraction is instead obtained from the pre-generated database via linear interpolation between the stored deadman states by the means of the liquid mass in the system m_{sys} , as

$$\epsilon = \lambda \epsilon_i + (1 - \lambda) \epsilon_{i+1}, \tag{10}$$

where i denotes the database entry i and λ the weight factor

$$\lambda = \frac{m_{i+1} - m_{\text{sys}}}{m_{i+1} - m_i}, \tag{11}$$

with $m_i \leq m_{\text{sys.}} < m_{i+1}$. Consequently, a sufficient number of deadman states need to be stored to avoid excessive smearing of the void fraction. Furthermore, $m_{\text{sys.}}$ is recalculated each time step by a summation over all cells as

$$m_{\text{sys.}} = \sum_{\text{cells}} \epsilon_j \rho_{f,j} V_j, \tag{12}$$

where index j denotes cell j and V_j its volume.

The particle–fluid momentum exchange term \mathbf{F}^{pf} is evaluated as

$$\mathbf{F}^{\text{pf}} = -\epsilon \beta \mathbf{u}_{\text{rel.}}, \tag{13}$$

where β is the drag induced momentum exchange coefficient. To preserve consistency with our previous work, β is modeled with the Koch and Hill drag relation [45,46] as

$$\beta = \frac{18\mu_f \epsilon^2 \epsilon_p}{d_p^2} \left(F_0(\epsilon_p) + \frac{1}{2} F_3(\epsilon_p) Re_p \right) \tag{14}$$

$$Re_p = \frac{\epsilon_p |\mathbf{u}_{\text{rel.}}| d_p}{\nu_f} \tag{15}$$

$$F_0(\epsilon_p) = \begin{cases} \frac{1 + 3\sqrt{\frac{\epsilon_p}{2}} + \frac{135}{64} \epsilon_p \ln(\epsilon_p) + 16.14\epsilon_p}{1 + 0.681\epsilon_p - 8.48\epsilon_p^2 + 8.16\epsilon_p^3} & \text{if } \epsilon_p < 0.4 \\ \frac{10\epsilon_p}{\epsilon^3} & \text{if } \epsilon_p \geq 0.4 \end{cases} \tag{16}$$

$$F_3(\epsilon_p) = 0.0673 + 0.212\epsilon_p + \frac{0.0232}{\epsilon^5}, \tag{17}$$

where ϵ_p is the solids fraction defined as $\epsilon_p = 1 - \epsilon$. The particle diameter d_p is evaluated as the Sauter mean diameter, calculated and stored in the deadman database from the CFD–DEM simulations and treated in a similar way to ϵ in Eq. 10. With this approach we assume $\mathbf{u}_p = 0$ so that $\mathbf{u}_{\text{rel.}} = \mathbf{u}_f$. If we presume that the deadman descends at the same rate as the fluids, the deadman velocity can be estimated as $\mathbf{u}_p = \mathcal{O}(\mathbf{u}_{\text{t.h.}} \cdot 10^{-6})$, assuming $d_{\text{t.h.}} = \mathcal{O}(10^{-2} \text{ m})$ and $d_{\text{hearth}} = \mathcal{O}(10 \text{ m})$, where $\mathbf{u}_{\text{t.h.}}$ is the taphole velocity. This should be a fair assumption, especially close to the taphole where the majority of the momentum exchange occurs.

2.3. Taphole boundary conditions

In order to perform realistic BF tapping simulations, considering the transient behavior of the taphole is crucial. Nishioka et al. [11] concluded that temporal variations of the taphole length $L_{\text{t.h.}}$, taphole diameter $d_{\text{t.h.}}$, as well as the surface roughness $\epsilon_{\text{t.h.}}$, all affect the tapping rate, although variations of $d_{\text{t.h.}}$ had the greatest impact.

While the taphole could be accounted for by incorporating it into the computational domain, extremely small cells would be required to resolve the flow profile in it. Additionally, modeling of temporal variations would still be challenging because of re-meshing during the simulation to vary the size. Hence, we choose to approximate the taphole effects by introducing a set of boundary conditions for the pressure and void fraction. By analogy with the findings of Nishioka et al. [11], we only consider a time-varying $d_{\text{t.h.}}$ and use constant values for $L_{\text{t.h.}}$ and $\epsilon_{\text{t.h.}}$.

2.3.1. Pressure boundary condition

The outlet pressure is estimated as

$$p_{\text{outlet}} = p_0 + \Delta p_{\text{t.h.}}, \tag{18}$$

where p_0 is the ambient pressure and $\Delta p_{\text{t.h.}}$ the pressure drop in the taphole estimated from the well known Darcy–Weisbach equation [47]

$$\Delta p_{\text{pipe}} = f_D \frac{\mathbf{u}_f^2 \rho_f L_{\text{t.h.}}}{2d_{\text{t.h.}}}, \tag{19}$$

which relates the pressure drop in a full-flowing pipe due to friction losses with the flow velocity and geometric properties. To account for its erosion, the taphole diameter may be modeled as expanding with time, as an example linearly, as

$$d_{\text{t.h.}} = d_{0,\text{t.h.}} + \dot{d}_{\text{t.h.}} \Delta t_f, \tag{20}$$

where $d_{0,\text{t.h.}}$ refers to the initial drill diameter and $\dot{d}_{\text{t.h.}}$ the erosion rate. Note that $d_{\text{t.h.}}$ is a calculated entity and differs from the mesh-based outlet size. f_D is the Darcy friction factor which can be determined from the Colebrook–White equation [48]

$$\frac{1}{\sqrt{f_D}} = -2 \log \left(\frac{\epsilon_{\text{t.h.}}}{3.7d_{\text{t.h.}}} + \frac{2.51}{Re_f \sqrt{f_D}} \right) \tag{21}$$

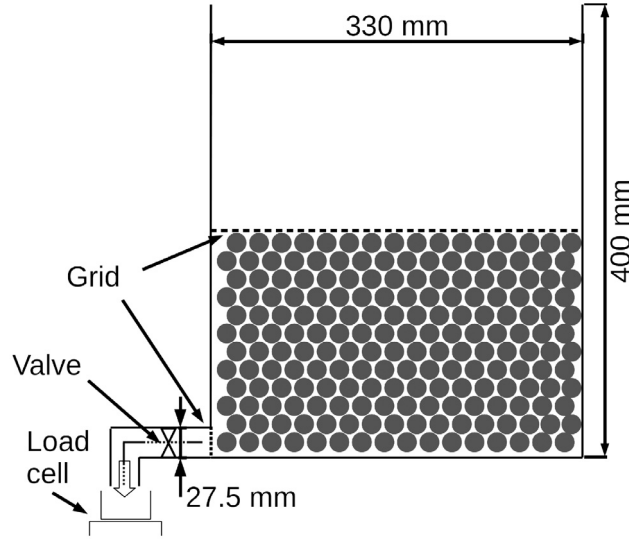


Fig. 3. Schematic illustration of the experimental setup used for validation. Water was drained through a wood particle bed from an outlet on the bottom left side with the drainage rate measured with a load cell. Two cases of a sitting and a floating bed were studied, where a grid was used in the sitting case to prevent the particles from floating up.

$$Re_f = \frac{\mathbf{u}_f d_{t,h.}}{\nu_f}. \tag{22}$$

However to avoid an iterative solution of Eq. (21) due to its implicit formulation, we used the explicit correlation proposed by Haaland [49]

$$\frac{1}{\sqrt{f_D}} = -1.8 \log \left[\left(\frac{\epsilon}{3.75 d_{t,h.}} \right)^{1.11} + \frac{6.9}{Re_f} \right]. \tag{23}$$

2.3.2. Void fraction boundary condition

While the pressure drop calculation was done using a temporally varying taphole size, the variations of the actual outlet size also had to be addressed. As previously stated, the exactness of the outlet size is crucial in order to obtain accurate tapping rates but it is not trivial how to consider the erosion effects.

In previous work we have successfully used the $\partial_n \epsilon|_{\text{outlet}} = 0$ boundary condition, which indicates that the tapping rate is determined from an effective outlet area $A_{\text{eff.}} = \epsilon A_{\text{outlet}}$, where ϵ is the void fraction in front of the taphole and A_{outlet} is the actual size of the mesh-based patch where the outflow condition is applied. Consequently, we propose altering of ϵ at the outlet boundary as

$$\epsilon \rightarrow \epsilon \frac{A_{t,h.}}{A_{\text{outlet}}}, \tag{24}$$

where $A_{t,h.} = \pi d_{t,h.}^2 / 4$ and A_{outlet} is the fixed outlet surface area.

3. Model validation

To assess the validity and functionality of the suggested model, we performed simulations using the dynamic void fraction model on our already existing experimental setup, schematically shown in Fig. 3. In these experiments, water was drained through a particle filled tank and the drainage rate as well as grain motion were monitored. Two cases were studied: a sitting and a floating particle bed, which had previously served for validation of the CFD–DEM model [24]. The geometry and initial states are shown in Fig. 4. The drainage was compared to the full CFD–DEM simulations and a parameter study was performed on the number of stored fields N_{fields} . Here, N_{fields} refers to the number of entries in the database described in Section 2. In this case, the database entries were not obtained from separate simulations without drainage, instead as we already had the solution of the full CFD–DEM simulation, they could directly be obtained at fixed intervals during the particle bed’s descent.

This simulation setup was also used to assess the proposed boundary conditions. The pressure boundary condition was evaluated by varying the virtual taphole length and studying its effect on the drainage rate. While this gave an indication of the boundary condition’s behavior, it requires actual validation in future work. The void fraction boundary condition, on the

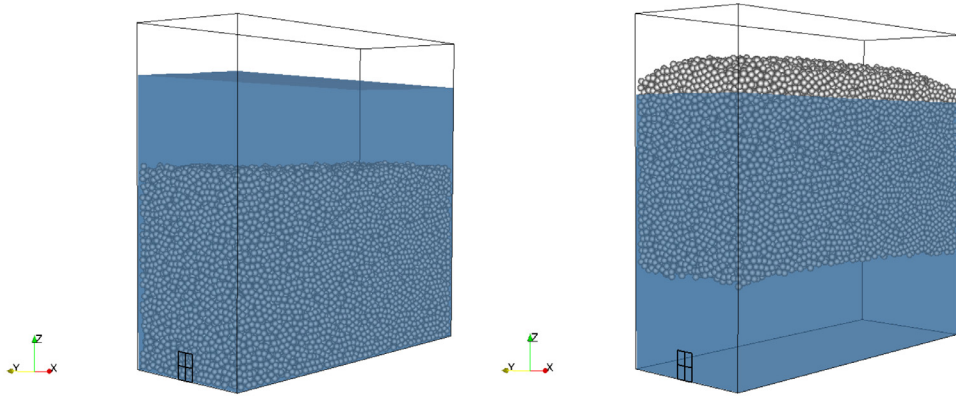


Fig. 4. Visualization of the initial states of the simulations for the sitting (left) and floating bed (right). In the latter case, the initial state was determined by the buoyancy of the submerged particles and the total bed weight. The outlet consisting of four cells was located on the bottom left side.

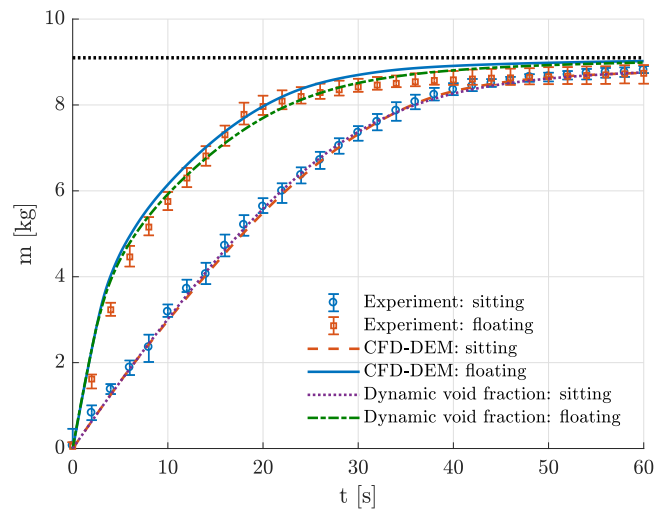


Fig. 5. Drained mass over time for the CFD-DEM model, dynamic void fraction model and experimental measurements. The simulation results are represented by lines and the measurements by error bars. The dotted black line indicates the initial amount of water in the tank.

other hand, was validated by applying it to the base case with the outlet size $d_0 = 27.5$ mm (here the subscript 0 emphasizes the base case) for various taphole sizes, and comparing the results to reference simulations with corresponding outlet sizes.

In our validation studies, we focused on the drained mass as an indicator for agreement between simulations and experiment. More detailed future investigations might also look at spatial details of the flow fields.

3.1. Results - model validation

Fig. 5 depicts the drainage over time for both the sitting and floating particle bed cases for the CFD-DEM as well as the dynamic void fraction model, compared with the experimental measurements. Here, we focus on the agreement between the two models and it is evident that in general good results are obtained. We see a perfect agreement for the sitting particle bed case, which confirms that the drag was successfully implemented in the Eulerian framework. In the floating particle bed case, we observe a slight deviation between the models occurring after $t \approx 5$ s. At that time, the particles started to reach the outlet and we ascribe the difference in drainage to the zero particle velocity assumption. As the particles approached the high fluid velocity region close to the outlet, the relative velocity was over-estimated as the particles were dragged with the fluid towards the outlet. The over-estimation of the relative velocity in turn resulted in excessive drag force which translated into the observed lower drainage rate. However, the deviation was small and we expect it to be even less prominent in the BF simulations, where the particle velocities are significantly lower.

In the simulation of the floating particle bed, we used a database consisting of $N_{\text{fields}} = 20$. **Fig. 6** shows snapshot comparisons of the void fraction between the CFD-DEM model and the dynamic void fraction model with $N_{\text{fields}} = 20$ and $N_{\text{fields}} = 3$, respectively, for two selected times. We observe that the dynamic void fraction model successfully captured the particle

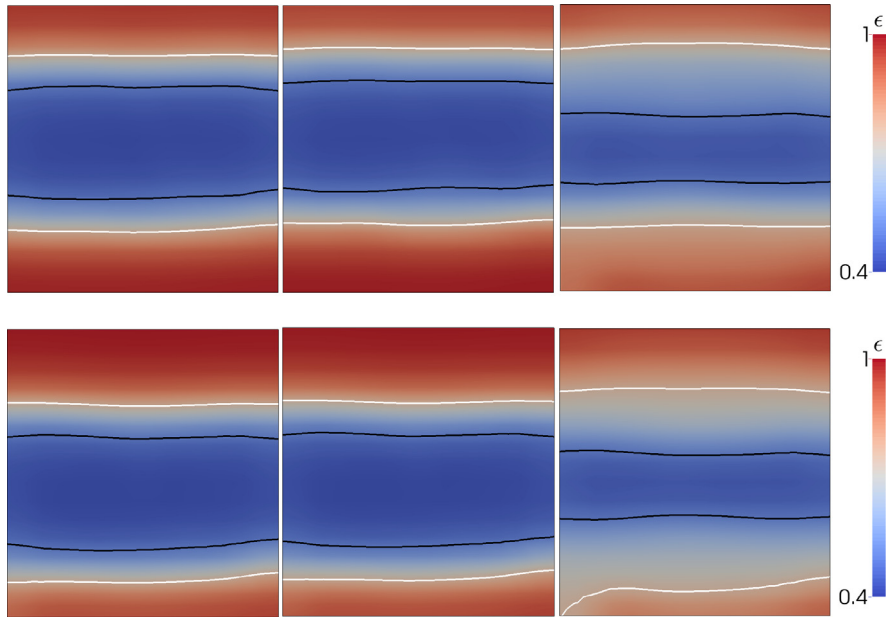


Fig. 6. Void fraction field for the CFD-DEM model (left), dynamic void fraction model with $N_{\text{fields}} = 20$ (middle) and with $N_{\text{fields}} = 3$ (right) at $t = 1$ s (upper row) and $t = 3$ s (lower row). The black and white lines represent the $\epsilon = 0.5$ and $\epsilon = 0.75$ isolines, respectively. The dynamic void fraction simulation with $N_{\text{fields}} = 20$ shows very good agreement with the full CFD-DEM simulation while the corresponding simulation with $N_{\text{fields}} = 3$ exhibits a heavily smeared void fraction field due to interpolation effects.

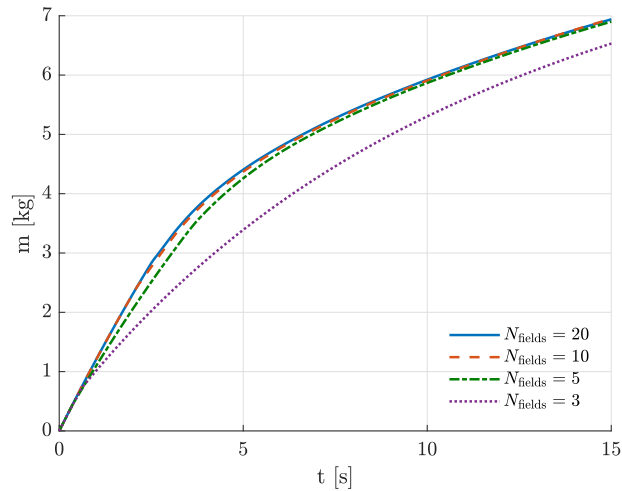


Fig. 7. Parameter analysis of N_{fields} on the initial drainage of the sitting particle bed simulation. As N_{fields} increases, the drainage starts to deviate because the flow faces earlier resistance due to interpolation effects close to the outlet.

bed’s descent towards the bottom of the tank. However, we see a strong smearing of the void fraction when $N_{\text{fields}} = 20$ was reduced to $N_{\text{fields}} = 3$ due to substantial interpolation effects.

The impact of interpolation errors on the drainage rate is depicted in Fig. 7 for a decreasing N_{fields} . It is evident that lower N_{fields} caused the curves to deviate early in the simulation because of slower drainage. Due to increasing interpolation errors with decreasing N_{fields} , the particle bed reached the outlet sooner, which in combination with high fluid velocities in the outlet’s vicinity imposed an earlier resistance to the flow.

3.2. Assessment of boundary conditions

The effect of the pressure boundary condition on the drainage is shown in Fig. 8. It is clear that the drainage rate decreased for increasing taphole lengths, which follows our intuitive expectations. We see that the resistance became noticeable when $L > 1$ m, which is in line with our experience from previous experiments.

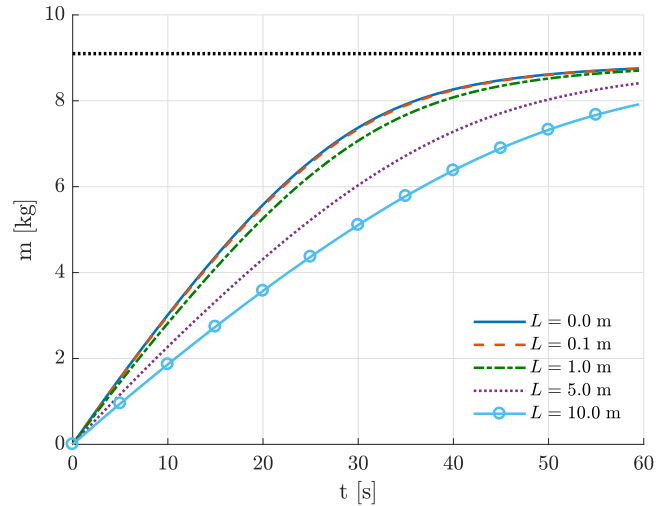


Fig. 8. Drained mass m over time for the sitting particle bed case with the pressure boundary condition applied, for a few various pipe lengths. The flow resistance is increasing for increasing L and appears to become significant when L exceeds one meter.

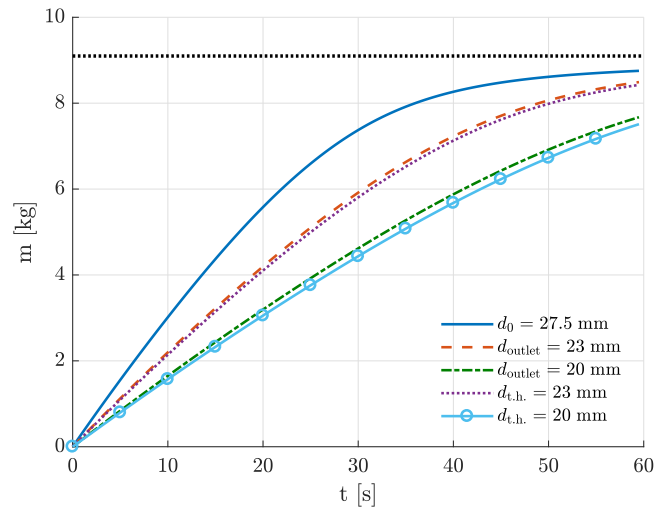


Fig. 9. A comparison of drained mass m over time for two outlet sizes d_{outlet} (re-meshing) with the usage of the void fraction boundary condition $d_{t,h}$ (no re-meshing). The boundary condition simulations were performed on the base case (d_0) mesh. In general, the effect of the desired outlet size was approximated satisfactorily, however the results indicate an increasing error for increasing $d_0/d_{t,h}$ ratios.

Fig. 9 depicts the drainage for simulations using the void fraction boundary condition of various taphole diameters, compared with corresponding reference simulations where the mesh-based outlet size was altered. In general, a good agreement is observed with an indication of an expectedly increasing error for larger $d_0/d_{t,h}$ ratios. Throughout the simulations, we encountered a maximum relative error of less than five percent, suggesting that the approach is reasonable for small $d_0/d_{t,h}$ ratios (tested up to $d_0/d_{t,h} \approx 1.9$).

4. Full-scale BF demonstration cases

In this section, we demonstrate the model in a BF hearth geometry at isothermal conditions, covering the procedure from generation of the deadman database to running the long-term dynamic void fraction simulation. We test the model on two different deadman conditions: a uniform one with a single particle size and one with a dense core of smaller particles. The latter is used to mimic the effect of particle fragmentation in the center due to e.g. poor coke quality and high mechanical stresses.

We stress that numerical simulations always involve some degree of abstraction and simplification, especially when they focus on novel computational techniques instead of gradual improvements of existing ones. In particular, we consider cold, isothermal conditions in contrast to hot particles and liquids, the latter being possibly subject to solidification at the walls. Furthermore, our geometry approximating the hearth with a cylindrical shape (cf. Section 4.1) is much simpler than that of

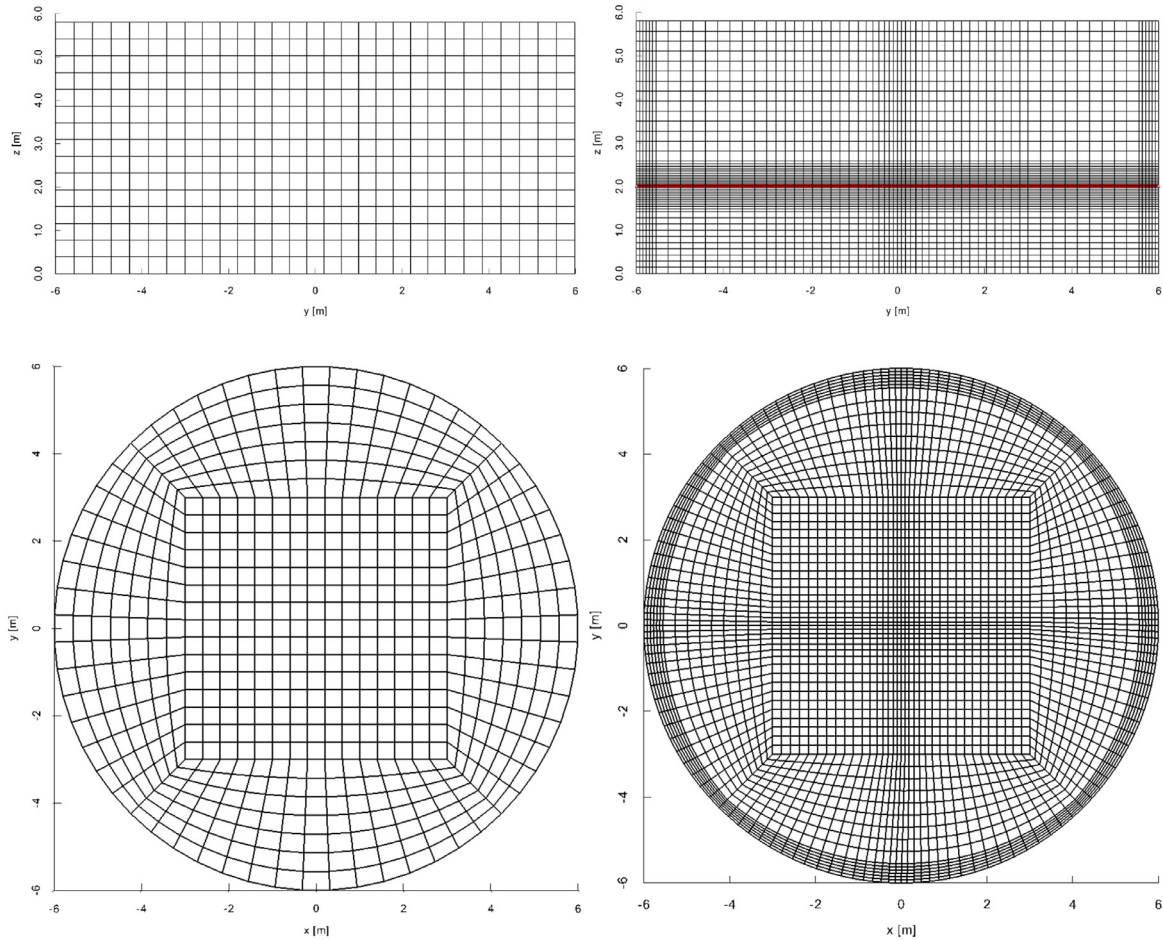


Fig. 10. Visualization of the mesh used in the CFD-DEM simulation (left) and with the dynamic void fraction (right). The figures in the upper row represent the central x -plane, and the lower row, the top view of the z -plane. The mesh on the right side is refined around the taphole level (red line), where we expected the greatest velocities and interface curvature. (For interpretation of the references to color in this figure legend, the reader is referred to the web version of this article.)

a real BF involving e.g. the “elephant foot”, a characteristic corrosion profile where the side walls meet the bottom. In our simulations, walls have no thickness, they simply confine the computation domain, which necessitates a specific boundary condition for the taphole (cf. Section 2.3) which is located rather low in our study. Finally, a real furnace contains particles with a broad range of sizes, and they can exhibit various types of structural changes like fragmentation or dissolution. As discussed in Section 4.2.1, we approximate a broad distribution with a coarse-grained, narrow one that additionally accounts for a higher packing fraction. Grains are assumed to be inert, although slow variations of the properties could be integrated easily.

Another simplification concerns the treatment of iron and slag generation. In reality, ore particles melt in the cohesive zone and the resulting liquids trickle down through the coke bed where they coexist before the droplets reach the bulk liquids. In our simulations, on the other hand, we neglect this trickling process and put mass sources in the domains occupied by iron and slag, respectively.

4.1. Geometry and mesh

We used an example furnace hearth modeled as a cylinder with the diameter $d_{\text{hearth}} = 12$ m and the height $h_{\text{hearth}} = 5.8$ m. The base mesh consisted of 9675 hexahedral cells, as shown on the left side in Fig. 10, which was used in the CFD-DEM simulations. In Ref. [24], we reported a major challenge regarding cell sizes inherent to the VOF-DEM coupling. In short, sacrifices have to be made to the flow resolution, which yield heavily smeared interfaces, as a certain minimum cell size is required in order to obtain a proper average representation of the discrete particles [32,50,51].

Table 1
Force wall parameters.

	$i = 1$	$i = 2$	$i = 3$	$i = 4$	$i = 5$
r_i [m]	0	1.2	2.4	3.6	4.8
R_i [m]	1.2	2.4	3.6	4.8	6.0
p_i [bar]	1.7	1.3	0.6	0.2	0.1

In the dynamic void fraction model, the grid size is no longer restricted as the particles are omitted, which enabled us to refine the mesh to 166250 cells (right side of Fig. 10), particularly close to the taphole, where we expected the greatest velocities and interfacial curvature.

4.2. Generation of deadman databases

In this section we present how to set up the CFD–DEM simulations in order to generate the deadman database using our suggested approach. Choices regarding particle sizes and burden weight distribution are discussed.

4.2.1. Particle sizes

To construct the uniform deadman, we used coke particles with $d_p = 60$ mm and $\rho_p = 1000$ kg/m³. To speed up the simulations, we employed coarse-graining, where a group of particles is represented by a single, larger one to reduce their number [25,27,52]. By using a coarse graining factor $CG = 2.5$, their total number was reduced from $N_p \approx 3.6 \cdot 10^6$ to $N_p \approx 230\,000$. The dense-core deadman also consisted of $d_p = 60$ mm particles except in the center, where $d_p = 30$ mm was used. Similarly here, coarse-graining was applied with $CG = 2.5$, resulting in $N_p \approx 460\,000$ for the dense-core deadman case.

So far, we had only considered mono-sized particles with different sizes in different zones, while in reality the deadman would be described by a (or several) size distribution(s). In general, poly-disperse systems have higher random close packing (RCP) fractions as a result of smaller particles filling the voids between the larger ones [53]. To address strong polydispersity, some of us [54] recently presented a method where an actual, broad size distribution with the random close packing $\alpha_{\text{full}}^{(\text{RCP})}$ is represented by a reduced, narrow one with $\alpha_{\text{red}}^{(\text{RCP})}$. Put differently, the influence of the smallest particles is accounted for by scaling the solids fraction and particle densities as

$$\epsilon_p = \epsilon_p \left(\left\{ d_p \cdot \left(\alpha_{\text{full}}^{(\text{RCP})} / \alpha_{\text{red}}^{(\text{RCP})} \right)^{1/3} \right\} \right) \quad (25)$$

$$\rho_p = \rho_p \alpha_{\text{full}}^{(\text{RCP})} / \alpha_{\text{red}}^{(\text{RCP})}. \quad (26)$$

In this work, we used the arbitrary $\zeta = \alpha_{\text{full}}^{(\text{RCP})} / \alpha_{\text{red}}^{(\text{RCP})} = 1.2$ in the dense center to demonstrate the method and highlight its effect on the flow. However, effective algorithms exist to calculate $\alpha^{(\text{RCP})}$ for given size distributions [54,55].

4.2.2. Burden weight approximation

As can be seen in our simulation domain setup, we neglected the remainder of the BF above the hearth. Consequently, the weight of the burden had to be approximated at the cut-off location and be applied to the particles because in combination with the buoyancy forces, it determined the position of the deadman. In our previous work [24], we proposed a method where a set of force walls was used to apply an estimated radial weight distribution. Such a wall mimics a specified force in a given direction, and by using a set of them, a distribution can be approximated. Determining the weight distribution itself is not trivial because the total weight of the burden, lift forces from the hot blast and wall effects all contribute to the effective downward force at the cut-off location. It could be approximated with a simple parameterized model as done by Brännbacka and Saxén [56], or potentially obtained from a full-BF DEM simulation [16,57,58]. Because this was beyond the scope of this work, we chose the pressure profile such that desirable initial states were achieved. Five force walls were used with the parameters listed in Table 1, where i denotes the different annular walls, with r and R representing the inner and outer radius respectively.

4.2.3. Short-term CFD–DEM simulations

Eight short-term simulations were performed with the initial liquid levels varying between $z_{0,\text{iron}} = 1.75 - 3.5$ m and $z_{0,\text{slag}} = 2.25 - 4.0$ m. The two extreme states, i.e. a sitting and a floating deadman, are depicted in Fig. 11 for both the uniform and dense-core cases. A summary of the fluid and particle simulation parameters are listed in Tables 2 and 3. The physical properties should not be considered as universal values because they depend heavily on parameters such as chemical composition and temperature and vary not only between different BFs but also between different operating conditions. The surface tension values listed in Table 2 represent the surface tension when exposed to air, and the iron-slag surface tension was approximated as the difference between the two values according to Antonoff's rule [59]. Although the effect of surface tension is included in our calculations via Eq. (5), we believe that the investigation of phenomena where it plays a critical role requires a highly detailed treatment that resolves the flow field below the particle scale.

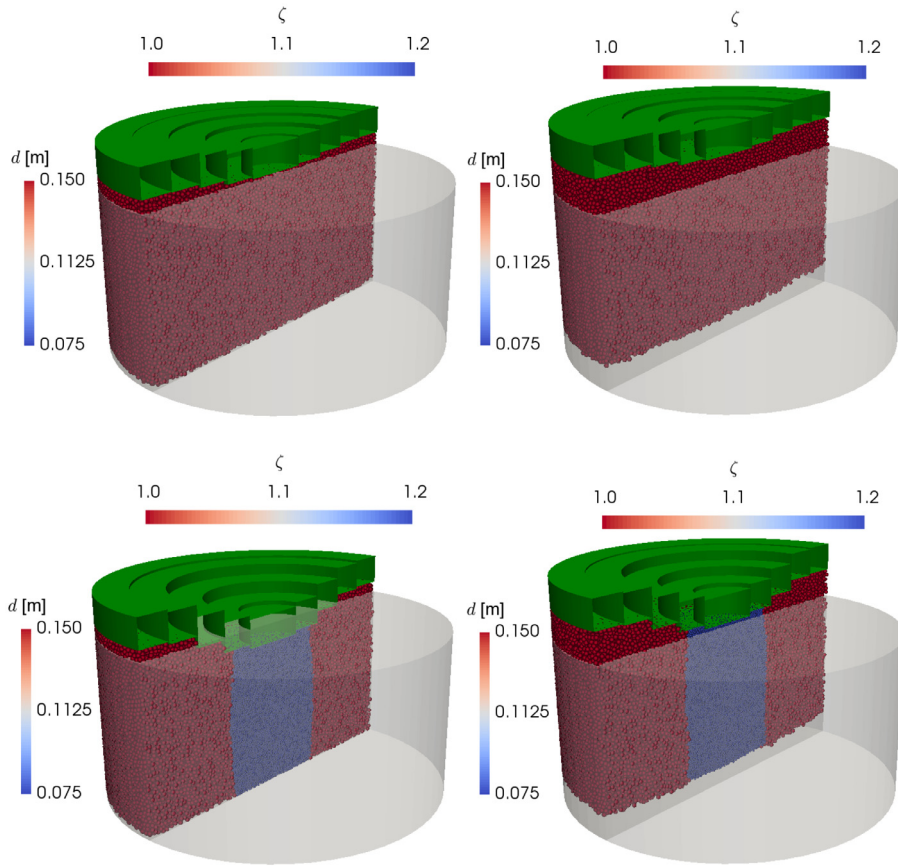


Fig. 11. Illustration of the two extreme deadman states: sitting (left column) and floating (right column), of the uniform case (upper row) and dense core (lower row). The green objects represent force walls used to mimic the downward acting force of the burden. These, along with six intermediate states were used to assemble the deadman database for the long-term simulations. (For interpretation of the references to color in this figure legend, the reader is referred to the web version of this article.)

Table 2
List of simulation parameters for the fluids.

Property	Value
Δt_r [s]	$5 \cdot 10^{-3}$
ρ_{iron} [kg/m ³]	7000
ρ_{slag} [kg/m ³]	2400
ρ_{air} [kg/m ³]	1.0
ν_{iron} [m ² /s]	$8.7 \cdot 10^{-7}$
ν_{slag} [m ² /s]	$1.25 \cdot 10^{-4}$
ν_{air} [m ² /s]	$1.3 \cdot 10^{-5}$
σ_{iron} [N/m]	1.65
σ_{slag} [N/m]	0.5

Table 3
List of simulation parameters for the particles.

Property	Uniform	Dense core
Δt_p [s]	$2.5 \cdot 10^{-4}$	$1.25 \cdot 10^{-4}$
ρ_p [kg/m ³]	1000	1000
d_p [mm]	150	75/150
N_p [-]	~230 000	~460 000
CG [-]	2.5	2.5
ζ [-]	1.0	1.2/1.0
Young's modulus, E [Pa]	$1.0 \cdot 10^8$	$1.0 \cdot 10^8$
Poisson's ratio, ν_p [-]	0.45	0.45
Coefficient of restitution, e [-]	0.3	0.3
Coefficient of friction, μ_p [-]	0.5	0.5

Table 4
List of taphole parameters.

Property	Value
$d_{0,t,h}$ [mm]	65
$d_{t,h}^i$ [m/s]	$1.0 \cdot 10^{-6}$
$L_{t,h}$ [m]	3.0
$\epsilon_{t,h}$ [mm]	0.015
p_0 [Pa]	0

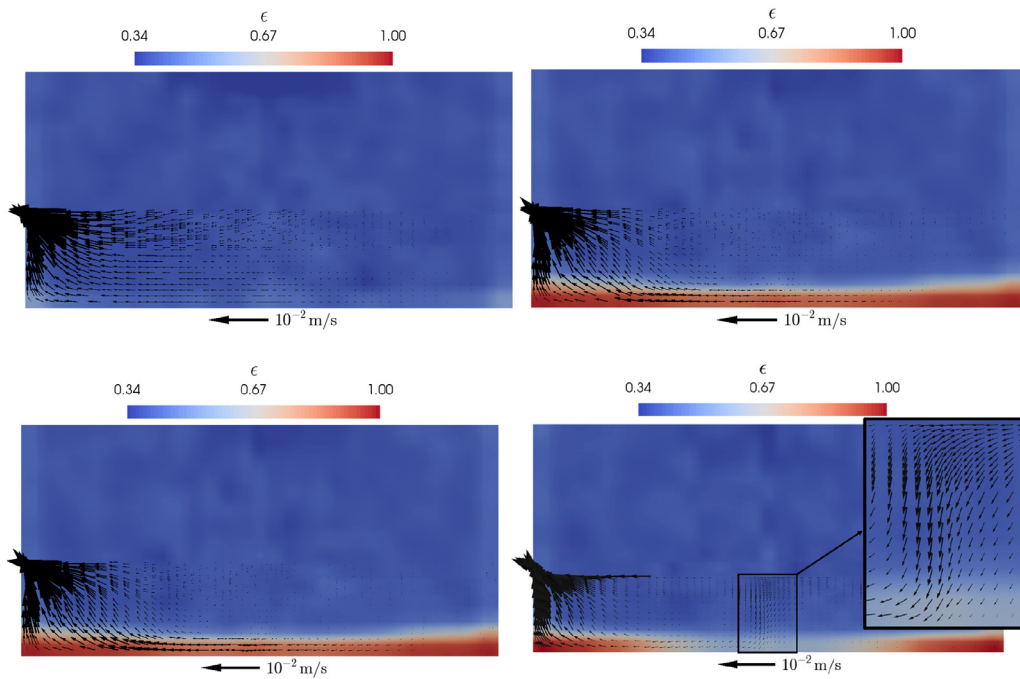


Fig. 12. Comparison of iron velocities in a cross-section normal to the taphole. In the upper row, snapshots are shown for a fixed sitting (left) and a fixed floating (right) deadman. The lower row visualizes the flow from early (left) and late (right) in the dynamic void fraction simulation. It can be seen that the coke free space caused by the floating deadman yielded high velocities close to the bottom. Additionally, the flow field changed during tapping with the dynamic deadman, as the deadman descended to a final partially floating state, which suppressed near-bottom flow far from the taphole (cf. close-up). Velocities exceeding $1.0 \cdot 10^{-2}$ m/s close to the taphole are filtered in order to aid visualization of the low velocities.

4.3. Dynamic void fraction model simulation setup

The long-term simulations were performed on the fine grid from Fig. 10 using the fluid properties from Table 2, with the initial iron level $z_{0,iron} = 2.5$ m and slag layer thickness $h_{0,slag} = 1.0$ m. The iron production rate was set to a constant $\dot{m}_{iron} = 150$ t/h with a slag ratio of $\gamma = 300$ kg/thm. The end of the tap was defined as when the criterion $\alpha_{air} \geq 0.5$ was fulfilled at the outlet. The taphole was located at $z_0 = 2.0$ m with the properties listed in Table 4 used for the outlet boundary conditions.

4.4. Long-term simulation results

Fig. 12 depicts the velocity fields in a cross-section normal to the taphole for a fixed sitting and static floating deadman (upper row). The fixed states were obtained by only using the deadman database entries corresponding to the extreme deadman states shown in Fig. 11. The floating deadman gave rise to a coke free space at the bottom wall, in which we observed high velocities. This behavior was in good agreement with the isothermal results reported by Guo et al. [4]. The increased velocities close to the bottom also caused more vertical motion of the flow close to the taphole. The lower row depicts snapshots of the iron flow field with the dynamic deadman model from early in the tapping (left) and towards the end (right). We see that the deadman was initially fully floating and towards the end it had descended to a partially floating state, where it sat in the center but not towards the side wall. As expected, the initial flow looks very similar to the fixed floating case, whereas towards the end, the high velocities close to the bottom wall have disappeared. The main iron flow appears to come from below the taphole with some downward motion in the center, which suggests a peripheral flow at the bottom.

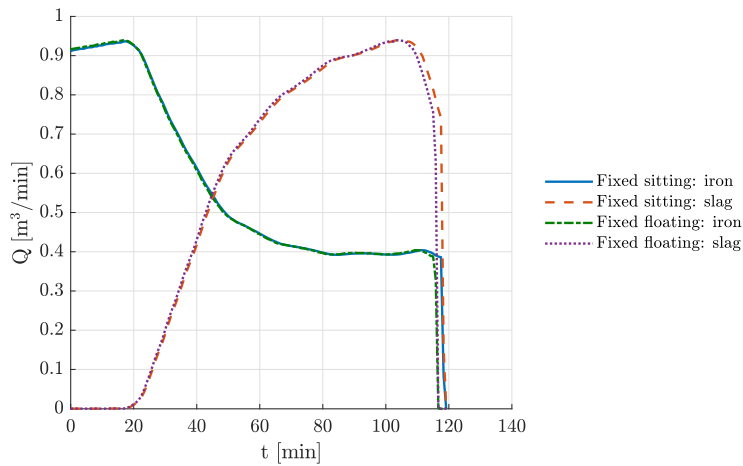


Fig. 13. Comparison of volumetric flow rate over time between a fixed sitting and a floating deadman. The drainage profiles look almost identical, indicating that the drainage rate was determined by the taphole properties and the porosity in front of the taphole.

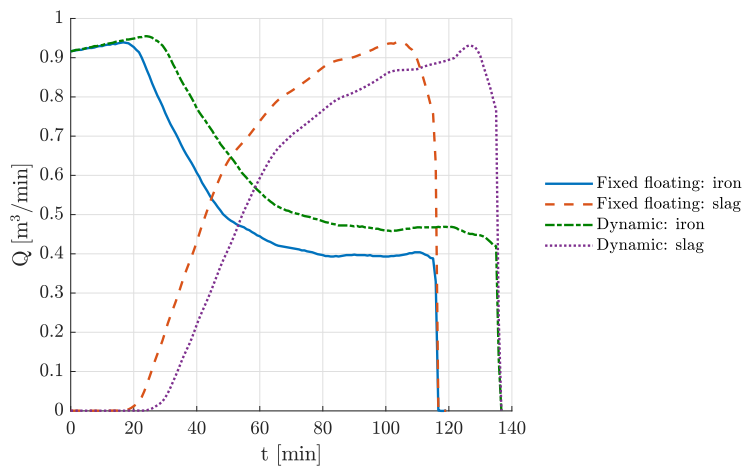


Fig. 14. Volumetric flow rate over time for a fixed floating deadman compared with a dynamic one. In the latter case, the iron flow rate was generally higher while that of slag was lower. Altogether, the fluid displacement of the deadman movement resulted in an extended tapping duration.

Fig. 13 shows the monitored iron and slag flow rates for a fixed sitting and floating deadman. We see an initially increasing iron rate due to the expanding taphole, which after approximately 20 min started to decrease as slag began to flow out. The slag drainage rate continued to increase until the end of the tap at about 120 min. Evidently, the drainage profiles for the fixed cases were virtually identical, which strengthens the statement that the drainage rate is mainly determined by the taphole properties [12]. However, we also experienced a strong dependence of the porosity in front of the taphole on the drainage rate with our set of boundary conditions (Section 2.3).

More interestingly, when we compare the drainage between a dynamic deadman and a fixed floating one as shown in Fig. 14, we see large differences. Seemingly, the descending deadman caused an increased iron flow and a decreased slag rate throughout the simulation. As the descending deadman displaced iron, the iron level remained higher and thus an increased slag delay as well as an extended tapping duration of about 20 min were observed.

Fig. 15 visualizes the evolution of the normalized averaged iron level and slag layer thickness. In both the fixed floating and dynamic deadman cases, we see a linearly increasing slag layer thickness until it peaks when the slag drainage rate equaled the production rate. With the dynamic deadman, we find a shift and increase of this peak due to the changed slag drainage behavior observed in Fig. 14. The iron level decreased rapidly until it approached the taphole level and we notice the well-known phenomenon that iron was drained from below the taphole. Although the tapping duration was different between the simulations, they culminate in similar final states with a iron level approximately 7 cm below taphole level and a residual slag thickness of about 30 cm. This is further highlighted in Fig. 16, where the slag and iron interfaces are visualized at a cross-section normal to the taphole for both the fixed floating and dynamic deadman simulations. We observed both the well-known downwards tilting of the slag interface towards the taphole, as well as the upwards tilting of the iron interface as iron was being drained from below taphole level. Although the expected trends were present, it should

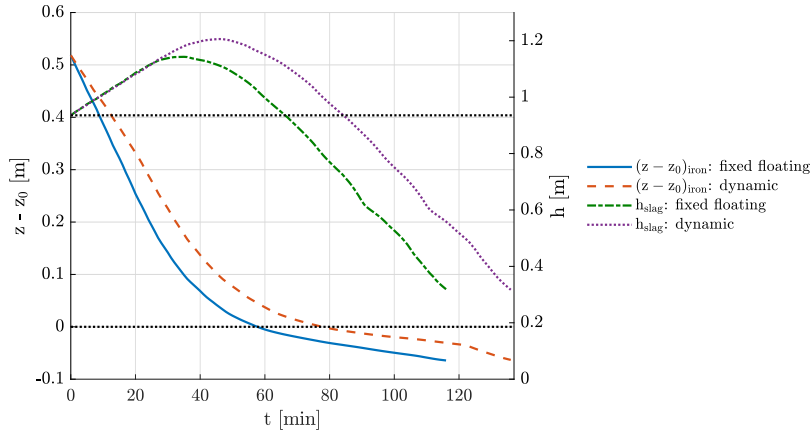


Fig. 15. Average iron level (left axis) and average slag layer thickness (right axis) over time. The black dotted lines represent the taphole level (lower) and the initial slag thickness (upper). A comparison is made between a fixed floating deadman and a dynamic one. Beyond the increased tapping duration, we observe an increase of peak slag layer thickness as well as that iron is drained from below the taphole.

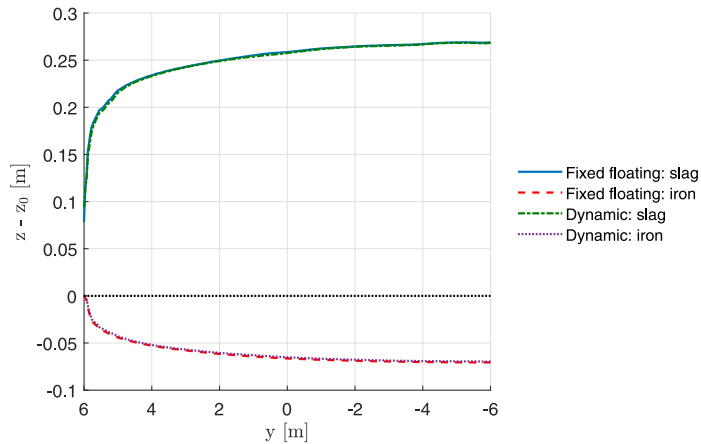


Fig. 16. Comparison of slag and iron interfaces in a cross-section normal to the taphole between a fixed floating and a dynamic deadman, at the end of respective tap. In both cases, we see the well known phenomena of both a downwards tilting slag interface towards the taphole, as well as the iron being drained from below taphole level. Despite the difference in drainage behavior, the final interfaces look almost identical.

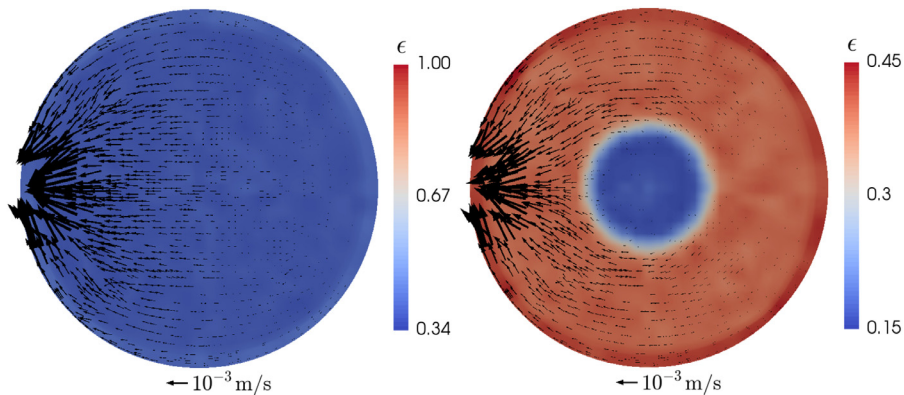


Fig. 17. A comparison of velocity fields on a horizontal plane at the taphole level for a uniform deadman (left) and one with a dense core(right). The uniform deadman shows an even velocity distribution while the almost impermeable center caused a peripheral flow pattern. Velocities exceeding $2.5 \cdot 10^{-3}$ m/s close to the taphole are filtered in order to aid visualization of the low velocities.

be stated that the exact interface location was heavily dependent on the grid resolution and smearing of the interface, especially close to the taphole with strong interfacial curvatures.

Beside the influence of a dynamic over a static deadman, we also briefly investigated the significance of its morphology. While no thorough analysis of several porosity distributions was performed, we want to accentuate the ease with which the model accounts for large inhomogeneities to the porosity. Snapshots of the velocity fields for the uniform- and dense core deadman are shown in Fig. 17 on a horizontal plane at taphole level. We see that the inclusion of the smaller particles and $\xi = 1.2$ in the center significantly reduced the permeability. While this did not directly affect the drainage, it promoted a peripheral hot metal flow pattern which could influence the refractory wear behavior.

5. Conclusion and outlook

In this work we presented the *dynamic void fraction model* which intends to enable full-scale BF hearth simulations over relevant time scales while taking the transient behavior of the deadman into account. By utilizing a CFD–DEM method, different deadman states were generated based on given coke particle size and burden weight distributions, resulting in more realistic inhomogeneous porosity fields. Interpolation between the deadman states was used in a long-term simulation to describe the deadman motion during a full tapping period. The model was validated on an experimental setup that we had also used in Ref. [24], where water was drained through a particle-filled tank.

In order to enable more realistic BF drainage simulations, we suggested a set of outlet boundary conditions to account for the transient behavior of the taphole. By approximating the outlet boundary pressure from theory of pressure drop in pipes, we obtained a temporally varying pressure as a function of the fluid Reynolds number and physical taphole properties. This formulation allowed for a simple, time-dependent description of taphole properties, e.g. length and diameter. Additionally, by adjusting the porosity at the outlet, we altered the effective outlet size to account for the increase of the taphole due to erosion. This proved to be accurate in our validation case with a maximum error in the order of 5% for $d_{\text{outlet}}/d_{\text{t.h.}} \approx 2$.

We demonstrated our model in a full-scale example BF for two different deadman setups: a uniform one with a single particle size and a polydisperse one with a dense center. As expected, the dynamic void fraction model turned out to be computationally much cheaper than CFD–DEM calculations. In particular, polydisperse particle size distributions which pose a major challenge for CFD–DEM did not add any significant costs. Compared to the CFD–DEM simulation for the dense-core case, we measured a speed-up of 5 with the dynamic void fraction model (both simulations utilized 32 CPUs). However, a direct comparison of the performance was difficult to obtain. While the dynamic void fraction model's computational time was primarily affected by the cell number N_{cells} , that of the CFD–DEM calculation approximately scaled with N_p . Additionally, by refining the mesh and reducing the particle size, the computational times did not only increase due to greater N_{cells} and N_p , but also because smaller fluid and particle time steps had to be taken to ensure numerical stability. Also, the one-time cost of generating the deadman databases should be taken into consideration, albeit it was small when everything was regarded. Altogether, it is evident that the dynamic void fraction model was significantly faster than the CFD–DEM model and enabled us to study full tapping cycles on fine meshes.

More specifically, we compared simulations of a static floating deadman with a dynamic one. We showed that initially, the flow fields between the two were almost identical, while towards the end of the tap, the dynamic deadman reached a partially floating state causing a different iron flow pattern. Comparing the drainage rates, we observed an increased iron and decreased slag flow rate throughout the simulation due to displacement of iron by the descending deadman. Consequently, we not only found an increased slag delay and maximum slag layer thickness, but also an extended tapping duration.

In this work, we chose to model the production of iron and slag via evenly distributed source terms throughout each phase, while in reality, both are produced in the cohesive zone and drip through the coke bed until they reach the hearth. It may be doubted if this behavior can be accounted for with the shared velocity field of the VOF approach. Furthermore, neglecting the incoming fluids' momentum could potentially affect the flow in the low velocity regions.

Future work should not only consider a more realistic implementation of the iron and slag production, but more importantly, it should incorporate the significant effects of natural convection [4,14]. This will require a model extension with multiphase heat transfer between the fluids as well as with the deadman, which will finally allow us to compare our model's predictions to real BF operational data. Furthermore, despite a good agreement was found between the simulations and experiments in the small-scale simplified case, the model should be validated in a real BF setup by e.g. comparing it with actual BF measurements to ensure its reliability in such a setting.

Acknowledgments

The research leading to these results has received funding from the European Union's Research Fund for Coal and Steel (RFCS) research programme under *grant agreement* no RFSR-CT-2015-00001.

References

- [1] M. Geerdes, H. Toxopeus, C. van der Vliet, *Modern Blast Furnace Ironmaking: An Introduction*, second ed., IOS Press, 2009.
- [2] L. Shao, *Model-based estimation of liquid flows in the blast furnace hearth and taphole*, Åbo Akademi University, 2013 Ph.D. thesis.
- [3] Y. Zhang, R. Deshpande, D.F. Huang, P. Chaubal, C.Q. Zhou, Numerical analysis of blast furnace hearth inner profile by using CFD and heat transfer model for different time periods, *Int. J. Heat Mass Transf.* 51 (1–2) (2008) 186–197.

- [4] B.Y. Guo, D. Maldonado, P. Zulli, A.B. Yu, CFD modelling of liquid metal flow and heat transfer in blast furnace hearth, *ISIJ Int.* 48 (12) (2008) 1676–1685.
- [5] D.F. Huang, F. Yan, P. Millovachi, P. Chaubal, C.Q. Zhou, Numerical investigation of transient hot metal flows in a blast furnace hearth, in: *Proceedings of the AISTech 2005*, Charlotte, 1, 2005, pp. 199–207.
- [6] S. Kuang, Z. Li, A. Yu, Review on modeling and simulation of blast furnace, *Steel Res. Int.* 89 (1) (2018) 1700071.
- [7] C.Q. Zhou, D.F. Huang, Y. Zhao, P. Chaubal, Computational fluid dynamics analysis of 3d hot metal flow characteristics in a blast furnace hearth, *J. Therm. Sci. Eng. Appl.* 2 (1) (2010) 011006.
- [8] D. Maldonado, P. Zulli, B.Y. Guo, A.B. Yu, Mathematical modelling of flows and temperature distributions in the blast furnace hearth, in: *Proceedings of the Fifth International Conference on CFD in the Process Industries*, Melbourne, 2006, pp. 1–6.
- [9] C.M. Chang, W.T. Cheng, C.E. Huang, S.W. Du, Numerical prediction on the erosion in the hearth of a blast furnace during tapping process, *Int. Commun. Heat Mass* 36 (5) (2009) 480–490.
- [10] D.F. Huang, Y. Zhang, R. Deshpande, P. Chaubal, C.Q. Zhou, Simulation of the hearth draining process and thermal stress of a BF hearth, in: *Proceedings of the AISTech 2007*, Indianapolis, 2007, pp. 475–485.
- [11] K. Nishioaka, T. Maeda, M. Shimizu, A three-dimensional mathematical modelling of drainage behavior in blast furnace hearth, *ISIJ Int.* 45 (5) (2005) 669–676.
- [12] K. Nishioaka, T. Maeda, M. Shimizu, Effect of various in-furnace conditions on blast furnace hearth drainage, *ISIJ Int.* 45 (10) (2005) 1496–1505.
- [13] T. Nouchi, M. Yasui, K. Takeda, Effects of particle free space on hearth drainage efficiency, *ISIJ Int.* 43 (2) (2003) 175–180.
- [14] J. Post, T. Peeters, Y. Yang, M. Reuter, Hot metal flow in the blast furnace hearth: Thermal and carbon dissolution effects on buoyancy, flow and refractory wear, in: *Proceedings of the Third International Conference on CFD in the Minerals and Process Industries*, Melbourne, 2003, pp. 433–440.
- [15] T. Nouchi, T. Sato, M. Sato, K. Takeda, T. Ariyama, Stress field and solid flow analysis of coke packed bed in blast furnace based on DEM, *ISIJ Int.* 45 (10) (2005) 1426–1431.
- [16] Z. Zhou, H. Zhu, A. Yu, B. Wright, D. Pinson, P. Zulli, Discrete particle simulation of solid flow in a model blast furnace, *ISIJ Int.* 45 (12) (2005) 1828–1837.
- [17] Z. Zhou, H. Zhu, A. Yu, P. Zulli, Numerical investigation of the transient multiphase flow in an ironmaking blast furnace, *ISIJ Int.* 50 (4) (2010) 515–523.
- [18] Z.Y. Zhou, H.P. Zhu, B. Wright, A.B. Yu, P. Zulli, Gas-solid flow in an ironmaking blast furnace-II: Discrete particle simulation, *Powder Technol.* 208 (1) (2011) 72–85.
- [19] S. Natsui, S. Ueda, H. Nogami, J. Kano, R. Inoue, T. Ariyama, Dynamic analysis of gas and solid flows in blast furnace with shaft gas injection by hybrid model of DEM-CFD, *ISIJ Int.* 51 (9) (2011a) 51–58.
- [20] S. Natsui, H. Nogami, S. Ueda, J. Kano, R. Inoue, T. Ariyama, Simultaneous three-dimensional analysis of gas-solid flow in blast furnace by combining discrete element method and computational fluid dynamics, *ISIJ Int.* 51 (1) (2011b) 41–50.
- [21] T. Ariyama, S. Natsui, T. Kon, S. Ueda, S. Kikuchi, H. Nogami, Recent progress on advanced blast furnace mathematical models based on discrete method, *ISIJ Int.* 54 (7) (2014) 1457–1471.
- [22] A. Adema, DEM-CFD Modelling of the Ironmaking Blast Furnace, Delft University of Technology, 2014 Phd thesis.
- [23] F. Bambauer, S. Wirtz, V. Scherer, H. Bartusch, Transient DEM-CFD simulation of solid and fluid flow in a three dimensional blast furnace model, *Powder Technol.* 334 (2018) 53–64.
- [24] M. Vångö, S. Pirker, T. Lichtenegger, Unresolved CFD-DEM modeling of multiphase flow in densely packed particle beds, *Appl. Math. Model.* 56 (2018) 501–516.
- [25] C. Bierwisch, T. Kraft, H. Riedel, M. Moseler, Three-dimensional discrete element models for the granular statics and dynamics of powders in cavity filling, *J. Mech. Phys. Solids* 57 (1) (2009) 10–31.
- [26] M. Sakai, S. Koshizuka, Large-scale discrete element modeling in pneumatic conveying, *Chem. Eng. Sci.* 64 (3) (2009) 533–539.
- [27] D. Queteschiner, T. Lichtenegger, S. Schneiderbauer, S. Pirker, Coupling resolved and coarse-grain DEM models, *Part. Sci. Technol.* 36 (4) (2018a) 517–522.
- [28] D. Queteschiner, T. Lichtenegger, S. Pirker, S. Schneiderbauer, Multi-level coarse-grain model of the DEM, *Powder Technol.* 338 (2018b) 614–624.
- [29] T. Lichtenegger, S. Pirker, Recurrence CFD – A novel approach to simulate multiphase flows with strongly separated time scales, *Chem. Eng. Sci.* 153 (2016) 394–410.
- [30] F. Cecconi, M. Cencini, M. Falcioni, A. Vulpiani, Predicting the future from the past: an old problem from a modern perspective, *Am. J. Phys.* 80 (11) (2012) 1001–1008.
- [31] J.P. Eckmann, S.O. Kamphorst, D. Ruelle, Recurrence plots of dynamical systems, *Europhys. Lett.* 4 (9) (1987) 973–977.
- [32] C. Kloss, C. Goniva, A. Hager, S. Amberger, S. Pirker, Models, algorithms and validation for opensource DEM and CFD-DEM, *Prog. Comput. Fluid Dyn.* 12 (2–3) (2012) 140–152.
- [33] C. Goniva, C. Kloss, N.G. Deen, J.A.M. Kuipers, S. Pirker, Influence of rolling friction on single spout fluidized bed simulation, *Particology* 10 (5) (2012) 582–591.
- [34] P.A. Cundall, O.D.L. Strack, A discrete numerical model for granular assemblies, *Géotechnique* 29 (1) (1979) 47–65.
- [35] C. Martin, D. Bouvard, S. Shima, Study of particle rearrangement during powder compaction by the discrete element method, *J. Mech. Phys. Solids* 51 (4) (2003) 667–693.
- [36] K. Johnson, *Contact Mechanics*, Cambridge University Press, 1985.
- [37] Y. Tsuji, T. Tanaka, T. Ishida, Lagrangian numerical simulation of plug flow of cohesionless particles in a horizontal pipe, *Powder Technol.* 71 (3) (1992) 239–250.
- [38] P. Seil, S. Pirker, T. Lichtenegger, Onset of sediment transport in mono- and bidisperse beds under turbulent shear flow, *Comput. Part. Mech.* 5 (2) (2018) 203–212.
- [39] A. Di Renzo, F. Paolo Di Maio, An improved integral non-linear model for the contact of particles in distinct element simulations, *Chem. Eng. Sci.* 60 (2005) 1303–1312.
- [40] Z.Y. Zhou, S.B. Kuang, K.W. Chu, A.B. Yu, Discrete particle simulation of particle-fluid flow: model formulations and their applicability, *J. Fluid Mech.* 661 (2010) 482–510.
- [41] C.W. Hirt, B.D. Nichols, Volume of fluid (VOF) method for the dynamics of free boundaries, *J. Comput. Phys.* 39 (1) (1981) 201–225.
- [42] T.B. Anderson, R.O.Y. Jackson, A fluid mechanical description of fluidized beds, *Ind. Eng. Chem. Fundam.* 6 (4) (1967) 527–539.
- [43] H. Rusche, *Computational fluid dynamics of dispersed two-phase flows at high phase fractions*, Imperial College London (University of London), 2002 Ph.D. thesis.
- [44] J.U. Brackbill, D.B. Kothe, C. Zemach, A continuum method for modeling surface tension, *J. Comput. Phys.* 100 (2) (1992) 335–354.
- [45] R.J. Hill, D.L. Koch, A.J.C. Ladd, The first effects of fluid inertia on flows in ordered and random arrays of spheres, *J. Fluid Mech.* 448 (2001) 213–241.
- [46] M.S. van Buijtenen, W.J. van Dijk, N.G. Deen, J. Kuipers, T. Leadbeater, D.J. Parker, Numerical and experimental study on multiple-spout fluidized beds, *Chem. Eng. Sci.* 66 (11) (2011) 2368–2376.
- [47] G.O. Brown, The history of the Darcy-Weisbach equation for pipe flow resistance, *Environ. Water Resour. Hist.* 38 (7) (2002) 34–43.
- [48] C.F. Colebrook, C.M. White, Experiments with fluid friction in roughened pipes, *Proc. R. Soc. Lond. A* 161 (906) (1937) 367–381.
- [49] S.E. Haaland, Simple and explicit formulas for the friction factor in turbulent pipe flow, *J. Fluid Eng.* 105 (1) (1983) 89–90.
- [50] L. Jing, C.Y. Kwok, Y.F. Leung, Y.D. Sobral, Extended CFD-DEM for free-surface flow with multi-size granules, *Int. J. Numer. Anal. Methods Geomech.* 40 (2016) 62–79.
- [51] J.M. Link, L.A. Cuypers, N.G. Deen, J.A.M. Kuipers, Flow regimes in a spout-fluid bed: a combined experimental and simulation study, *Chem. Eng. Sci.* 60 (13) (2005) 3425–3442.

- [52] S. Radl, C. Radeke, J.G. Khinast, S. Sundaresan, Parcel-based approach for the simulation of gas-particle flows, Proceedings of the Eighth International Conference on CFD in Oil & Gas, Metallurgical and Process Industries, Trondheim (2011) 1–10.
- [53] K.W. Desmond, E.R. Weeks, Influence of particle size distribution on random close packing of spheres, *Phys. Rev. E* 90 (2) (2014) 1–6.
- [54] T. Lichtenegger, S. Pirker, CFD-DEM modeling of strongly polydisperse particulate systems, *Powder Technol.* 325 (2018) 698–711.
- [55] R.S. Farr, R.D. Groot, Close packing density of polydisperse hard spheres, *J. Chem. Phys.* 131 (24) (2009) 244104.
- [56] J. Brännbacka, H. Saxén, Model analysis of the operation of the blast furnace hearth with a sitting and floating dead man, *ISIJ Int.* 43 (10) (2003) 1519–1527.
- [57] A.T. Adema, Y. Yang, R. Boom, Discrete element method-computational fluid dynamic simulation of the materials flow in an iron-making blast furnace, *ISIJ Int.* 50 (7) (2010) 954–961.
- [58] Z. Zhou, H. Zhu, A. Yu, B. Wright, P. Zulli, Discrete particle simulation of gas-solid flow in a blast furnace, *Comput. Chem. Eng.* 32 (8) (2008) 1760–1772.
- [59] H. Kim, D.J. Burgess, Prediction of interfacial tension between oil mixtures and water, *J. Colloid Interface Sci.* 241 (2) (2001) 509–513.